Available online at www.sciencedirect.com
SCIENCE DIRECT®
International Journal of Heat and Mass Transfer 47 (2004) 3431–3439
International Journal of HEAT and MASS TRANSFER
www.elsevier.com/locate/ijhmt

A numerical study on the flow over a novel tube for heat-transfer enhancement with a linear Eddy-viscosity model

Wen-Lih Chen [a,*], Zengyuan Guo [b], Cha'o-Kuang Chen [c]

[a] Department of Mechanical Engineering, KSUT, 949, Da Wan Rd., Yung-Kang City, Tainan Hsien 710, Taiwan
[b] Department of Engineering Mechanics, Tsinghua University, Beijing 100084, China
[c] Department of Mechanical Engineering, NCKU, Tainan, Taiwan

Received 19 September 2003; received in revised form 11 January 2004
Available online 9 April 2004

Abstract

A computational study is presented which analyzes details of the flow and heat-transfer behaviors in a novel heat-transfer-enhancement tube with a low-Reynolds number turbulence model. The tube is constructed with a series of alternative vertically and horizontally positioned oval pipes connected by transition sections, which bridge a vertically positioned cross-section to a horizontally positioned one, or vice versa. Results are presented for local as well as overall flow and heat-transfer parameters, including skin-friction coefficient and Nusselt number. It is found that the transition sections contribute most to the promotion of heat-transfer but with the penalty of producing the largest pressure drop per unit length. The geometry of the transition section tends to provoke separation bubbles, which not only attenuate local heat-transfer rate but also result in higher pressure-loss. The study demonstrates that, within the range of Reynolds numbers investigated, this new configuration can largely enhance heat-transfer from 40% to over 100% comparing to a circular pipe. However, the price is that the pressure drop caused by the former is also generally twice as much as that of the latter.

1. Introduction

Heat-transfer enhancement has been an active and important subject for many decades. It concerns fundamentally the performance of a wide range of industrial devices, especially heat exchangers. Hence, any improvement of the heat-transfer performance of these devices implicates great economical potential. Conventionally, problems associated with heat-transfer are classified into internal/external flow, forced/natural convection or boundary layer/separated flow, etc., and researchers tend to conclude that heat-transfer coefficient *Nu* can be expressed as a function of Reynolds number *Re*, Grashof number *Gr* and Prandtl number *Pr* [1–5]. However, Tao et al. [6] indicated that *Nu* is not only dependent on fluid velocity and properties, which are used to derived non-dimensional parameters *Re*, *Gr* and *Pr*, but also closely related to the state of the fluid flow. From energy equation, it can be readily demonstrated the mechanism of convective heat-transfer goes hands in hands with the coordination of velocity and temperature fields. This concept offers a better understanding of a number of heat-transfer phenomena, and most importantly, the development of new heat-transfer enhancement approaches. As shown in Fig. 1(a), a staggered oval pipe is an example of one of such approaches to improve the heat-transfer rate in heat exchangers. This configuration can be used to construct tube bank in boilers, to replace circular pipes in condensers or evaporators in air conditioners, or any device, which includes pipes in its heat-exchange components. Guo [7] measured such a staggered oval pipe, which enhances heat-transfer up to 300% compared with a circular pipe with only a moderate penalty of increase in skin-friction between 30% and 120%. This demonstrates the favorable heat-transfer performance of such configuration and its economical

* Corresponding author. Fax: +886-6-2050509.
E-mail address: wlchen@mail.dwu.edu.tw (W.-L. Chen).

0017-9310/$ - see front matter © 2004 Elsevier Ltd. All rights reserved.
doi:10.1016/j.ijheatmasstransfer.2004.01.014

Nomenclature

c_μ, f_μ	coefficients in Eddy-viscosity relation	β	thermal expansions coefficient of air
g	gravity acceleration	σ_k, σ_ε, σ_t	diffusion coefficients for k, ε, and t equations, respectively
k	turbulence energy		
p	pressure	δ_y	normal distance from the wall
Re	Reynolds number	ε	dissipation rate of k
T	temperature	$\tilde{\varepsilon}$	homogeneous dissipation rate of k
u_i	velocity vector	μ_t, ν_t	dynamic and kinematic turbulence viscosity
x_i	Cartesian coordinates	ρ	fluid density

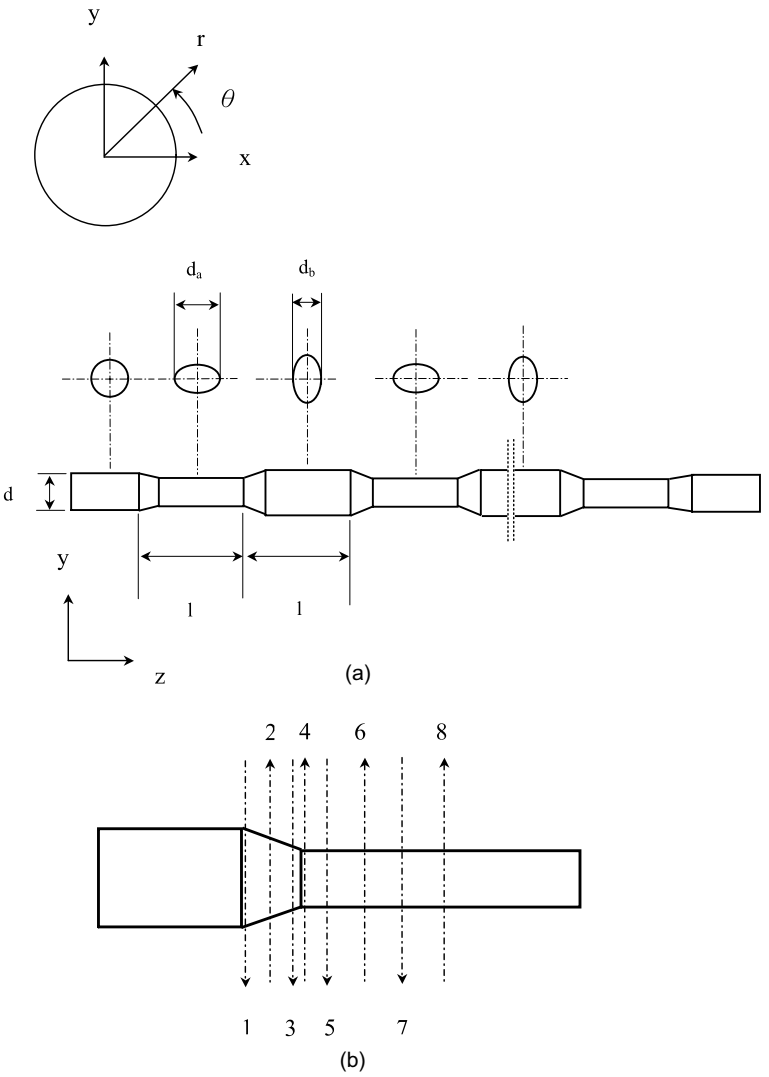

Fig. 1. The geometry configuration of the staggered oval pipe, (a) overall view, and (b) the positions of eight different locations.

potential. However, Guo's measurement does not include either details of the flow and temperature fields or discussions on the most important factors contributing to heat-transfer enhancement. This paper studies the flow in Guo's experiment numerically, aiming to provide details of the flow inside such a configuration and, most

importantly, analyze local as well as overall heat-transfer behaviors along the pipe to identify the most significant heat-transfer promoting factors.

Since the geometry of the current configuration is complicated, containing discontinue geometry curvature prone to create localized circulation bubbles, this paper employs a low-Reynolds number turbulence model to resolve the details inside the separation bubble and the near-wall region. A low-Reynolds number model requires particular fine near-wall mesh to achieve y^+ of the first near-wall cell the order of unity. Such a fine near-wall mesh naturally provides good numerical accuracy to resolve skin-friction as well as wall heat flux.

2. Turbulence model

The well-known low-Reynolds number k–ε model of Launder and Sharma [8] is adopted in this study. This model has been tested against a wind range of flows [9]. Although its predictive accuracy is not always satisfactory, it at least demonstrates the ability to capture important flow phenomena in most flow conditions. To this end, the Navier–Stokes equations together with Launder–Sharma model can be written as

$$\frac{\partial}{\partial x_i}(\rho u_i) = 0 \tag{1}$$

$$\rho\frac{\partial u_i}{\partial t} + \rho u_i\frac{\partial u_i}{\partial x_i} = -\frac{\partial p}{\partial x_i} + \frac{\partial}{\partial x_i}\left[(\mu+\mu_t)\frac{\partial u_i}{\partial x_i}\right] \tag{2}$$

The energy equation is

$$\frac{\partial T}{\partial t} + u_i\frac{\partial T}{\partial x_i} = \frac{\partial}{\partial x_i}\left[\left(\alpha + \frac{\nu_t}{\sigma_t}\right)\frac{\partial T}{\partial x_i}\right] \tag{3}$$

where $\alpha = \frac{\kappa}{\rho C_p}$. The equations for turbulence energy k and its homogeneous dissipation rate $\tilde{\varepsilon} \equiv \varepsilon - \left(\frac{\partial\sqrt{k}}{\partial x_i}\right)^2$ are

$$\rho\frac{\partial k}{\partial t} + \rho u_i\frac{\partial k}{\partial x_i} = \frac{\partial}{\partial x_i}\left[\left(\mu + \frac{\mu_t}{\sigma_k}\right)\frac{\partial k}{\partial x_i}\right] + P_k - \rho\varepsilon \tag{4}$$

$$\rho\frac{\partial \tilde{\varepsilon}}{\partial t} + \rho u_i\frac{\partial \tilde{\varepsilon}}{\partial x_i} = \frac{\partial}{\partial x_i}\left[\left(\mu + \frac{\mu_t}{\sigma_\varepsilon}\right)\frac{\partial \tilde{\varepsilon}}{\partial x_i}\right] + \rho\frac{\tilde{\varepsilon}}{k}(c_{\varepsilon 1}P_k - c_{\varepsilon 2}f_2\tilde{\varepsilon}) + E \tag{5}$$

where $E = 2\mu\mu_t\left(\frac{\partial^2 u_k}{\partial x_i \partial x_j}\right)^2$. The Eddy-viscosity is obtained from

$$\mu_t = \rho c_\mu f_\mu \frac{k^2}{\tilde{\varepsilon}} \tag{6}$$

in which c_μ and f_μ are taken from the following value or function:

$$c_\mu = 0.09, \quad f_\mu = \exp\left[\frac{-3.4}{\left(1 + \widetilde{R}_t/50\right)^2}\right], \quad \widetilde{R}_t = \frac{\rho k^2}{\mu\tilde{\varepsilon}} \tag{7}$$

The model coefficients in the above equations are

$$\sigma_t = 0.9, \quad \sigma_k = 1.0, \quad \sigma_\varepsilon = 1.3, \quad c_1 = 1.44,$$
$$c_2 = 1.92, \quad f_2 = 1.0 - 0.3\exp(-\widetilde{R}_t^2) \tag{8}$$

No-slip condition has been applied on pipe's outer surface, resulting in

$$u_i = k = \tilde{\varepsilon} = 0 \tag{9}$$

3. Numerical framework

Calculation reported herein have been performed with the unstructured-mesh, fully collocated, finite-volume code, 'USTREAM' developed by the first named author. This is the descendent of the structured-mesh, multi-block code of 'STREAM' [10]. Convection of mean-flow as well as turbulence quantities is approximated with the scheme 'UMIST' [11], a second-order TVD implementation of the QUICK scheme of Leonard [12]. Within this scheme, the transport solutions and the pressure-correction equation are solved sequentially and iterated to convergence, defined by reference to Euclidean residual norms for mass, the moment components and the temperature. A fully implicit scheme, with the time variation approximated to second-order accuracy, is incorporated to solve unsteady problems.

The following describes the discretization practices of USTREAM. A general conservation equation in arbitrary coordinate system can be written as

$$\frac{\partial}{\partial t}(\rho\phi) + \mathrm{div}(\rho\vec{u}\phi - \Gamma_\phi\nabla\phi) = s_\phi \tag{10}$$

where ϕ stands for any of the independent variables u_i, k, ε, etc. and Γ_ϕ, s_ϕ are the associated diffusion and source coefficients, which can be deduced from the parent equations. By integrating Eq. (10) over an arbitrary volume V bounded by a closed surface S can be written as

$$\frac{\mathrm{d}}{\mathrm{d}t}\int_V \rho\phi\,\mathrm{d}V + \int_S(\rho\vec{u}\phi - \Gamma_\phi\nabla\phi)\cdot\mathrm{d}\vec{S} = \int_V s_\phi\,\mathrm{d}V \tag{11}$$

where $\vec{S}$ is the surface vector. If V and S are, respectively, taken to be the volume V_p and discrete faces S_j $(j = 1, N_f)$ of a computational cell, Eq. (11) becomes

$$\frac{\mathrm{d}}{\mathrm{d}t}\int_{V_p} \rho\phi\,\mathrm{d}V + \sum_{j=1}^{N_f}\int_S(\rho\vec{u}\phi - \Gamma_\phi\nabla\phi)\cdot\mathrm{d}\vec{S} = \int_{V_p} s_\phi\,\mathrm{d}V \tag{12}$$

From here onwards, approximations are introduced. The first term on the left-hand-side of Eq. (12) is discretized as

$$\frac{\mathrm{d}}{\mathrm{d}t}\int_{V_p}\rho\phi\,\mathrm{d}V \cong \frac{(\rho\phi V)_p^{\mathrm{n}} - (\rho\phi V)_p^{\mathrm{o}}}{\delta t} \tag{13}$$

where the superscripts n and o refer to 'new' and 'old' time levels, respectively, separated by an interval δt. The second left-hand-side of Eq. (12) is split into the separated contributions C_j and D_j due to convection and diffusion, respectively, and each is expressed in terms of averaged values over cell faces, denoted by $(\ )_j$ thus

$$\begin{aligned}\sum_{j=1}^{N_f}\int_S(\rho\vec{u}\phi-\Gamma_\phi\nabla\phi)\cdot\mathrm{d}\vec{S}&\cong\sum_{j=1}^{N_f}(\rho\vec{u}\phi\cdot\vec{S})_j-\sum_{j=1}^{N_f}(\Gamma_\phi\nabla\phi\cdot\vec{S})_j\\&\equiv\sum_{j=1}^{N_f}C_j-\sum_{j=1}^{N_f}D_j\end{aligned}\tag{14}$$

The diffusion terms D_j are approximated by face-centered expressions of the form

$$D_j\cong\Gamma_{\phi,j}\left[f_j^l(\phi_N-\phi_P)+\left\{\nabla\phi\cdot\vec{S}-f_j^l\nabla\phi\cdot\vec{d}_{PN}\right\}_j\right]\tag{15}$$

where the first term in the brackets represents the normal diffusion between cell-centered node P and the neighboring cell-centered node N and the second term within the curly bracket is the cross-diffusion term. Terms f_j are geometrical factors, $\vec{d}_{PN}$ is the distance vector between P and N, and $\Gamma_{\phi,j}$ is the interpolated face diffusivity.

4. Results and discussion

The geometry of the staggered elliptical pipe is shown in Fig. 1(a). As seen, the initial section is circular with d in diameter. It is bridged to a horizontally positioned elliptical section by a transition section. This horizontal section is then connected to a vertically positioned elliptical section, again, via another transition section. The pattern of alternating horizontal and vertical section arrangement is then repeating until end of the tube where the final section becomes circular again. Here, the long and short diameters of all elliptic sections are d_a and d_b, respectively, while the length of a section unit, including a transition section and a constant-area elliptic section, is l. In this paper the values of d, d_a, d_b, l and the length of a transition section l_t are 16.5, 20, 13, 40 and 6 mm, respectively. In computation, a uniform velocity u_0 with constant low fluid temperature T_L is specified at the inlet, while the tube wall is no-slip and maintained at a constant high temperature T_H. In this flow condition, Reynolds number Re is defined, according to the geometry of the initial circular-cross-section pipe, as $\frac{u_0 d}{\nu}$. This makes the entrance flow condition identical to a pure-circular pipe at the same Reynolds number thus facilitates the comparison of the heat-transfer performance between the staggered oval pipe and circular pipe. Since the geometry of the pipe's cross-section is symmetrical, only a quarter of the cross-section is adopted as the computational domain. Initial computation showed that both flow and temperature fields become periodical at the eighth section unit, hence, the final computational domain comprises 12 section units, among which the tenth unit is taken for the analytical purpose. Three different grid sizes have been constructed and tested with $Re = 20,000$ to identify an appropriate mesh size to achieve grid-independent solution. Results of this grid-independent test are given in Table 1. One can see that the differences of averaged Nusselt number and skin-friction coefficient obtained from the medium mesh and the finest mesh are all less than 1%, demonstrating that the medium mesh with $45\times30\times540$ in radial, circumferential, and axial directions, is fine enough to ensure a grid-independent solution. In this mesh, particular fine grid, 70 nodes, in axial direction are allocated to each of the final 4 section units, aiming to resolve details of some localized regions. Also, the averaged y^+ value with $Re = 60,000$ (the highest Reynolds number investigated in this paper) is only 0.89, indicating that the near-wall grid is fine enough to employ a low-Reynolds number model. The application of inlet and wall boundary conditions is straight forwards and needs no further description. A zero-gradient boundary condition is used for the exit. This seems to contradict with the periodical nature of the pipe. However, considering that the outlet flow condition is applied at the 12th section unit, located far downstream of the tenth section unit, which all the results are extracted from, one can expect that this flow condition would pose little effect on the results far upstream from its location, especially with Reynolds number at a fairly high level (the flow tends to show a parabolic behavior rather than an elliptic one).

Table 1
The results of the grid-independent test

Grid size	$Nu/Pr^{1/3}$	f
$30\times20\times300$	120.9	0.0605
$45\times30\times540$	111.76	0.0637
$60\times40\times700$	111.21	0.0642

Nu and f are defined in Eqs. (16) and (17), respectively.

As seen in Fig. 1(b), eight locations, where flow and temperature information will be extracted and post-processed, are then positioned along the axial direction of the tenth unit. Based on the local axial length of the tenth unit, the positions of these eight locations are $0.01l$, $0.075l$, $0.125l$, $0.175l$, $0.2l$, $0.325l$, $0.45l$ and $0.575l$, respectively. Among them, the first three positions are located in the transition section. In the following, computational results associated with the tenth

unit at flow condition of $Re = 20,000$ are presented in Figs. 2–6. Fig. 2 shows u–v velocity vectors and pressure-contours at the eight different locations. Here, the magnitude of the secondary flow in the horizontally positioned elliptic section is much smaller than that in the transition section, hence, the velocity vectors of locations 5–8 are plotted with a scale 1.6 times larger than that for the first four locations. Additionally, two cross-sections at $\theta = 90°$ and 0°, showing v–w and u–w velocity vectors, are given in Fig. 3. Fig. 4 shows the variations of the square of averaged velocity magnitude, averaged pressure and cross-section area along the axial

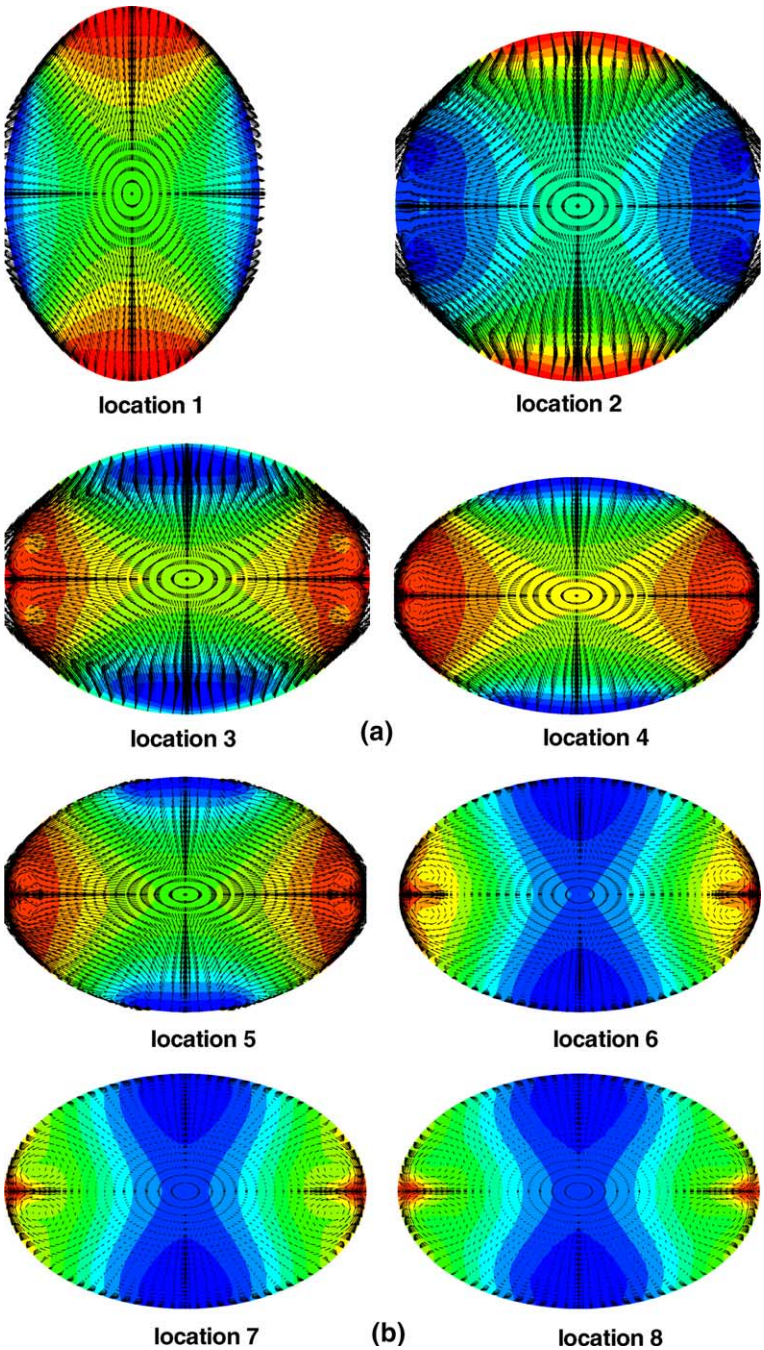

Fig. 2. Pressure-contours and velocity vectors at x–y plane for eight different locations; (a) locations 1–4, and (b) locations 5–8.

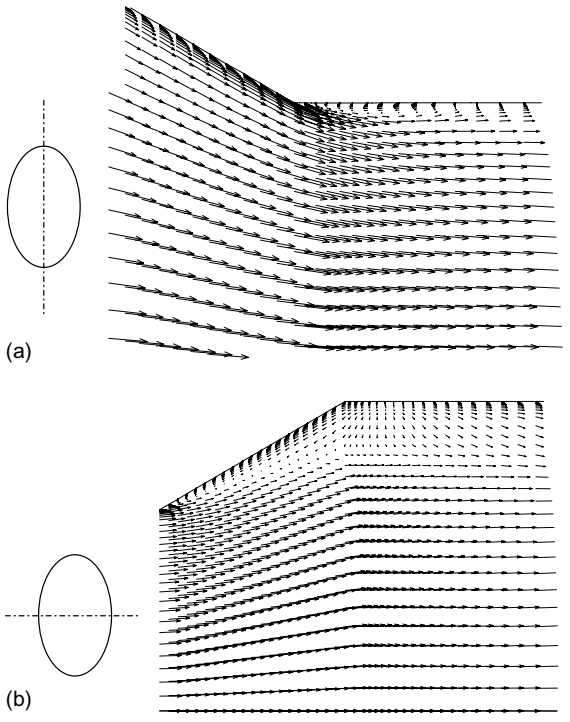

Fig. 3. Velocity vectors at (a) y–z plane, and (b) x–z plane.

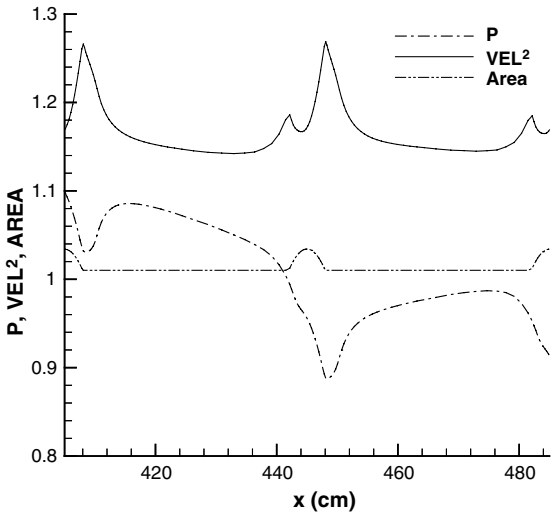

Fig. 4. Distributions of averaged pressure and velocity magnitude square along the axial direction.

direction for two section units, while variations of averaged Nusselt number in axial direction and distributions of local Nusselt number at some selected locations are plotted in Fig. 5. Here, Nusselt number is defined as follows:

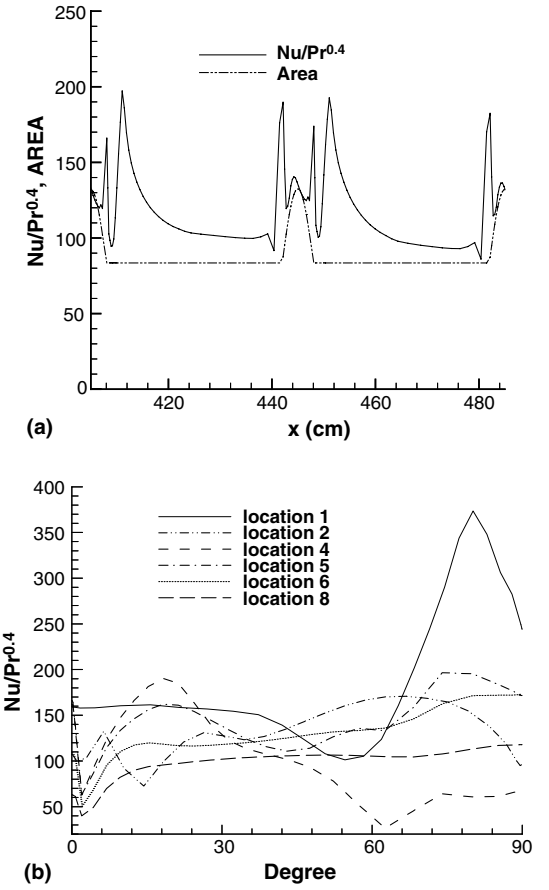

Fig. 5. Averaged and local Nusselt number distributions, (a) averaged Nusselt number distributions along the axial direction, and (b) local Nusselt number distributions at six different locations.

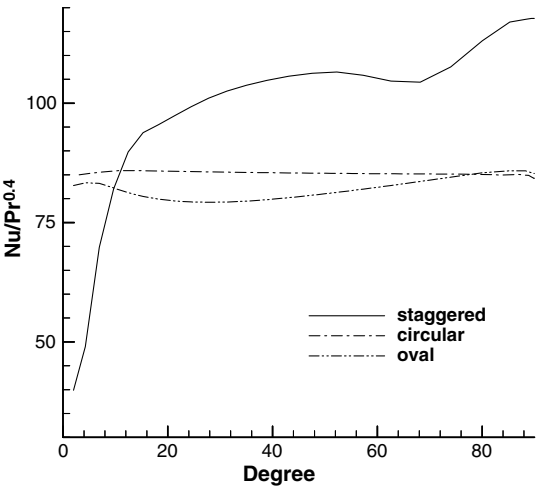

Fig. 6. Local Nusselt number distributions for staggered oval pipe, circular pipe and pure oval pipe at $Re = 20,000$.

$$Nu = \frac{q_w}{T_H - T_{ave}} \frac{d}{\kappa} \tag{16}$$

where q_w, T_{ave} and κ are wall heat flux, sectional averaged temperature and wall conductivity, respectively. Wall heat flux q_w is calculated as $q_w = \kappa \frac{\partial T}{\partial n}$, in which n is the normal direction from the wall surface.

As the tube's cross-section transforming from a vertically positioned elliptic to a horizontally positioned one in the transition section, the region near $\theta = 90°$, termed region 1, is compressed, whereas, the region near $\theta = 0°$, termed region 2, is expanding. From the velocity vector and pressure-contour plot at location 1 in Fig. 2(a), this geometry variation initially poses high pressure on the former region and low pressure at the later. The pressure difference then creates a strong secondary flow, driving fluid to flow from region 1 to 2. This flow pattern continues to the middle of the transition section, location 2 in Fig. 2(a). However, the effect of continuing compression at region 1 and expansion at region 2 acts to accelerate fluid flow at the former and decelerate fluid flow at the later. This results in gradually diminishing of pressure level at region 1, while building up pressure level at region 2. Eventually, pressure level at region 2 becomes larger than that of region 1 at the later stage of the transition section as seen from location 3 in Fig. 2(a). At this location, it is also noticeable that there is a vortex forming at region 2. Since $\theta = 0°$ is a symmetric plane where fluid cannot flow through, it can only curve backwards and hence form a vortex. This secondary flow pattern continues for a short length downstream the end of transition section as shown at locations 4 and 5 in Fig. 2(a) and (b). Further downstream (illustrated in Fig. 2(b), locations 6–8) one can see that the strength of secondary flow readily diminishes along the horizontally positioned elliptic section. Meanwhile, a second vortex is gradually developing near region 1 and becomes comparable, in terms of size, to that near region 2. Eventually, regarding a quarter of the cross-section, two major vortexes circulating at opposite direction form the main structure of the secondary flow at the later stage of the constant-area section. From the above discussion, one can readily realize that it is the transition section, which provides the driving force for the secondary flow.

Fig. 3 reveals details, especially the appearance of some separation regions, of the axial flow, which is of great importance to the heat transfer on the tube wall. The aforementioned geometrical contraction and expansion at the transition section near regions 1 and 2, respectively, are clearly seen in Fig. 3. The velocity vector in Fig. 3(a) shows flow acceleration exerted by the geometrical contraction. It also can be noted that there exists a separation bubble at the immediate downstream region of the transition-section exit. Evidently, this separation bubble is formed due to a discontinuity of geometrical curvature at the exit of the transition section. On the other hand, Fig. 3(b) indicates that the geometrical expansion produces a similar effect to a diffuser, which results in a massive separation region in the vicinity of wall at region 2. This separation region even extends into the constant-area section. A near-wall separation bubble is well-known to cause attenuation of wall heat flux at its vicinity, thus, to a certain extent, reduces the overall performance of the pipe. Therefore, any axial separation bubble needs to be avoided or reduced in size to improve overall heat-transfer rate. The actual effect of these separation bubbles on the heat-transfer performance of the current configuration will be discussed later.

The variations of averaged flow quantities along the axial direction shown in Fig. 4 reveal the significance of the effect created by transition section, thought short in length to the overall pipe. In the figure, the variation of cross-section area is also cross-plotted primary to provide visual reference to the axial location. Secondary, this quantity is directly linked to the variation of sectional-averaged velocity magnitude since the working fluid is incompressible. Hence, to see how it changes along the axial direction is important to understand the overall flow behavior. As seen in Fig. 4, the value of cross-section area only changes in transition section, in which it reaches its maximum value at the middle of the transition section, the location where the geometry of tube's cross-section becomes circular. Here, the sectional-averaged square of velocity magnitude, instead of velocity magnitude, is given since the latter is only a simple function of cross-section area. This quantity shows that flow begins to accelerate at the immediate upstream region of the transition section. The acceleration carries on a short range upon entering the transition region, and then the flow begins to decelerate due to the increase of cross-section area. The deceleration tendency continues until the middle of the transition section, where the maximum cross-section area is. Further downstream until the end of the transition section, the flow sharply accelerates again most likely due to the combined effects of flow acceleration near $\theta = 90°$, the displacement from the massive separation bubble near $\theta = 0°$, and the reduction of the cross-section area. Upon the exit of the transition section, the acceleration quickly loses its momentum and the flow decelerates almost all the way along the constant-area section. Also shown in this plot are the distributions of the sectional-averaged pressure, the quantity used to evaluate energy loss. It is readily seen that the sharpest drop of pressure level also occurs at the transition section, implying that this section is, on one hand, effective to promote flow acceleration and produce secondary flow but, on the other, responsible to the majority of energy loss.

Comparing the sectional-averaged Nusselt number distributions in Fig. 5(a) and the averaged square of

velocity magnitude in Fig. 4, one can see that these two quantities are, to some extent, correlated. However, the correlation is not good in transition section and the region immediate downstream of the transition section, places where separation bubbles exist. The attenuation effect of a separation bubble on the wall heat-transfer at its vicinity region can be realized by comparing the velocity vectors in Fig. 3(a) and the local Nusselt number distributions in Fig. 5(b). Fig. 3(a) shows that there exists a separation bubble immediate downstream of the transition section. The middle position of this separation bubble can be identified as location 4 in Fig. 1(b), and its corresponding local Nusselt number distributions are given in Fig. 5(b). These two plots indicate that the level of local Nusselt number is particularly low inside the separation bubble. The local Nusselt number distributions at location 4 further suggests that this separation bubble seems to cover an extensive region in the circumferential direction, from $\theta = 50°$ to 90° (regarding a quarter section). The overall effect of this separation bubble on the attenuation of heat-transfer can be fully understood from the axial Nusselt number distributions in Fig. 5(a). Here, the existence and the extension of this separation can be signified by the deep valley located immediate downstream of the transition section. Downstream the reattachment point of separation bubble, the level of Nusselt number quickly recovers, reaching a peak but begins to decline along the axial direction until the entrance of the next transition section.

Regarding the heat-transfer enhancement of the current staggered oval pipe configuration, Fig. 6 compares the local Nusselt number distributions from location 8, fully develop section from a circular pipe, and that from an oval pipe, all tested with the same flow condition. Even through the level of Nusselt number from location 8 is among the lowest within a section unit, it is clear that it still higher than those from the other two configurations, demonstrating the favorable heat-transfer performance of the current configuration. The averaged Nusselt number and skin-friction distributions of the current configuration and a circular pipe over a range of Reynolds numbers are given in Figs. 7 and 8, respectively. Here, skin-friction factor is calculated by estimating sectional pressure drop as follows:

$$f = \frac{\Delta p}{\frac{1}{2}\rho U_0^2}\frac{d}{l} \tag{17}$$

where, Δp is the pressure difference at the inlet and outlet of a section unit. While, the Nusselt number and skin-friction factor in circular tube are estimated from the following equations [1,13]:

$$Nu_s = \frac{\frac{f}{8}(Re-1000)Pr_f}{1+12.7\left(\frac{f}{8}\right)^{1/2}\left(Pr_f^{2/3}-1\right)}\left(\frac{Pr_f}{Pr_w}\right)^{0.11} \tag{18}$$

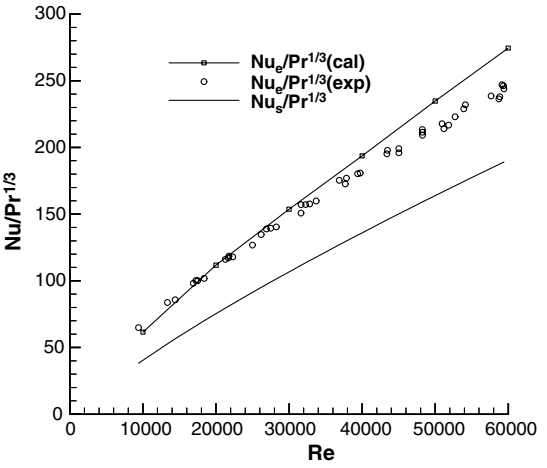

Fig. 7. Distributions of averaged Nusselt number at different Reynolds number for staggered oval pipe and circular pipe.

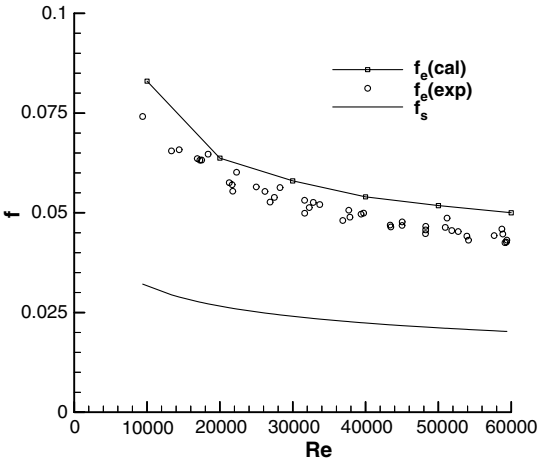

Fig. 8. Distributions of skin-friction coefficient at different Reynolds number for staggered oval pipe and circular pipe.

$$f_s = (0.79\ln(Re) - 1.64)^{-2} \tag{19}$$

From Figs. 7 and 8, the results show that the computational results are in good agreement with the data. Comparing to traditional tubes, the Nusselt number distributions shown in Fig. 7 indicate that this configuration can largely enhance heat-transfer, ranging from 40% to more than 100%, depending on Reynolds number. The effectiveness of heat-transfer enhancement is more pronounced at low Reynolds number than at high Reynolds number. However, this achievement does not come cheap. The penalty is its skin-friction level being generally two times higher than that from a circular pipe as shown in Fig. 8. Nevertheless, there is still potential to further improve the heat-transfer performance of a

staggered-oval pipe and reduce the pressure-loss, especially finding a geometry, which can reduce the sizes of separation bubbles.

5. Conclusions

A novel configuration of heat-transfer-enhancement pipe has been investigated numerically with a low-Reynolds number k–ε model. The computational results are in good agreement with the measurements. Comparing to a circular pipe, this configuration can raise averaged Nusselt number from 40% to more than 100% over a range of Reynolds number from 10^4 to 6×10^4. However, the penalty is that the level of pressure drop is also increased twice more than that of circular pipe in general. By examining the local heat-transfer coefficient along a section unit, it is found that the transition section, which connects two differently positioned oval sections, contributes most to the enhancement of heat-transfer. On the other hand, the middle of an oval section marks the lowest level of this quantity. However, even at this position, the level of local Nusselt number is still larger than that obtained from a circular pipe. Careful investigation of the flow field shows that there exist some separation bubbles at the transition sections. These separation bubbles not only increase the level of pressure drop but also largely reduce the local heat-transfer rate. This implies that the effectiveness of heat-transfer enhancement can be further improved and level of pressure drop diminished if the separation bubbles can be eliminated or reduced in size by modifying the geometry around the transition section. This is, however, beyond the scope of the current paper and remains one of the objectives of the future work.

Acknowledgements

The work reported herein was supported by a Taiwanese National Science Council funded project, numbered NSC-91-2212-E-434-001. The authors are grateful for this support.

References

[1] B.S. Petukhov, V.N. Popov, Theoretical calculation of heat exchange and frictional resistance in turbulent flow in tubes of an incompressible fluid with variable physical properties, High Temp. Heat Phys. 1 (1963) 69–83.
[2] P. Kumar, R.L. Judd, Heat transfer with coiled wire turbulence promoters, Can. J. Chem. Eng. 48 (1970) 378–383.
[3] R.L. Webb, in: Principles of Enhanced Heat Transfer, John Wiley and Sons Inc., New York, 1994, p. 89.
[4] Y. Fujita, A.M. Lopez, Heat-transfer enhancement of twisted-tap inserts in turbulent pipe flows, Heat Transfer—Jpn. Res. 24 (1995) 378–396.
[5] A.E. Bergles, Heat transfer enhancement—the measuring of the second-generation heat transfer technology, Heat Transfer Eng. 18 (1997) 47–55.
[6] W.Q. Tao, Z.Y. Guo, B.X. Wang, Field synergy principle for enhancing convective heat transfer—its extension and numerical verifications, Int. J. Heat Mass Transfer 45 (2002) 3849–3856.
[7] Z.Y. Guo, A brief introduction to a novel heat-transfer enhancement heat exchanger, internal report, Department of EMEMKLEHTEC, Tsinghua University, Beijing, China, 2003.
[8] B.E. Launder, B.I. Sharma, Application of the energy-dissipation model of turbulence to the calculation of flow near a spinning disc, Int. J. Heat Mass Transfer 1 (1974) 131.
[9] W.L. Chen, F.S. Lien, M.A. Leschziner, Non-linear Eddy-viscosity modeling of transitional boundary layers pertinent to turbomachine aerodynamics, Int. J. Heat Fluid Flow 19 (1998) 297–306.
[10] F.S. Lien, W.L. Chen, M.A. Leschziner, A multiblock implementation of a non-orthogonal, collocated finite volume algorithm for complex turbulent flows, Int. J. Numer. Meth. Fluids 23 (1996) 567–588.
[11] F.S. Lien, M.A. Leschziner, Upstream monotonic interpolation for scalar transport with application to complex turbulent flows, Int. J. Numer. Meth. Fluids 19 (1994) 527.
[12] B.P. Leonard, A stable and accurate convective modeling procedure based on quadratic upstream interpolation, Comput. Meth. Appl. Mech. Eng. 19 (1979) 59.
[13] V. Gnielinski, New equations for heat and mass transfer in turbulent pipe and channel flows, Int. Chem. Eng. 16 (1976) 359.